

The Stability Transition from Stable to Unstable Frictional Slip with Finite Pore Pressure

R. Affinito¹, C. Wood¹, S. Marty¹, D. Elsworth^{1,2}, C. Marone^{1,3}

¹Department of Geosciences, Pennsylvania State University

²Department of Energy and Mineral Engineering, EMS Energy Institute, and G3 Center, Pennsylvania
State University

³Dipartimento di Scienze della Terra, La Sapienza Università di Roma

¹Department of Geosciences, 503 Deike Building, University Park, PA 16802 USA

²EMS Energy Institute, Penn State University, C-211 Coal Utilization Laboratory, University Park, PA
16802 USA

³Department of Earth Sciences, La Sapienza University of Rome, P.le Aldo Moro, 5 - 00185 Rome, Italy

Key Points:

- Slow-slip events and the transition to dynamic stick-slip failure can occur for fluid-saturated faults.
- For granular fault zones sheared at low pore pressures, the frictional stability transition does not require dilatant hardening.
- Slow earthquakes and quasi-dynamic fault slip modes can be explained by strain rate dependence of the critical frictional weakening.

Abstract

Pore fluids are ubiquitous throughout the lithosphere and are commonly cited as the cause of slow-slip and complex modes of tectonic faulting. We investigate the role of fluids for slow-slip and the frictional stability transition and find that the mode of fault slip is mainly unaffected by pore pressures. We shear samples at effective normal stress (σ'_n) of 20 MPa and pore pressures P_p from 1 to 4 MPa. The lab fault zones are 3 mm thick and composed of quartz powder with median grain size of 10 μm . Fault permeability evolves from 10^{-17} to 10^{-19} m^2 over shear strains up to 26. Under these conditions, dilatancy strengthening is minimal. Slow slip may arise from dilatancy strengthening at higher fluid pressures but for the conditions of our experiments slip rate-dependent changes in the critical rate of frictional weakening are sufficient to explain slow-slip and the stability transition to dynamic rupture.

Plain Language Summary

Earthquakes begin and propagate within the fluid-saturated rocks of Earth's crust. Many investigators have suggested that high pore fluid pressure (Pp) is essential for slow earthquakes and tremor. These studies rely on the idea that changes in Pp can impact rupture propagation speed by dilatant volume increase during faulting with concurrent increases in fault normal stress. Thus, understanding the processes that produce slow-slip vs. dynamically propagating rupture is integral to seismic hazard forecasting. Here, we describe experiments on granular faults that produce the full spectrum of slip observed in nature. We measure the mechanical and hydraulic behavior of the faults and determine that frictional and fluid-driven processes occur in conjunction. Importantly, we demonstrate that frictional processes are sufficient to explain slow-slip and the transition to dynamic events without requiring Pp changes.

1 Introduction

Slow earthquakes and other quasi-dynamic modes of fault slip appear to be analogs of ordinary, elastodynamic earthquakes (Dal Zilio et al., 2020). Still, the mechanisms that dictate rupture propagation speed for slow events are poorly understood. In many cases, slow earthquakes occur at depths associated with metamorphic dehydration (Behr & Bürgmann, 2021) and alterations in permeable pathways (Williams, 2019), thus elevated pore pressure is commonly suggested as their cause (Condit & French, 2022). Additionally, laboratory studies have shown that rock fracture and fault slip can induce dilatancy and cause pore pressure to drop and faults to strengthen (Brantut, 2020). These observations are consistent with mechanisms such as seismic pumping, fault-valve behavior (Sibson, 1986), and dilational strengthening (Segall et al., 2010). However, it is often unclear whether dynamic fluid responses act to stabilize fault slip or destabilize via mechanisms such as thermal pressurization (Segall & Rice, 2006). Thus, details of slip-induced volume changes and fault permeability are essential to resolve these issues, yet poorly constrained.

From a frictional perspective, high pore pressure reduces fault strength, bringing it closer to failure (Hubbert & Rubey, 1959; Ellsworth, 2013). However, while the Coulomb-Mohr failure criterion predicts the stress state, it does not address the stability of frictional motion and whether slip will be seismic or aseismic. This is determined by fracture energy considerations and fluid-fault interactions such as storage capacity and fluid diffusion time (Biot, 1941). Thus, while fluids are clearly important, the wide range of conditions under which slow earthquakes occur (Sacks et al., 1978; Bürgmann, 2018) suggests that other mechanisms may play a role.

With the recognition that pore fluid pressures and their pathways are highly variable along subducting interfaces (Behr & Bürgmann, 2021), it may be appropriate to focus on whether changes in pore pressure result in modulation in the effective normal stress or are dissipated by fluid diffusion (Faulkner & Rutter, 2001). Dilational strengthening requires that increased pore volume *via* slip reduces the pore fluid pressure and thus temporarily increases the effective stress across the fault. The resultant change in stress effectively clamps the interface and arrests slip. Thus, it is often assumed as a potential mechanism for SSEs. Yet, the opposite mechanism can also occur, whereby undrained compaction leads to slip *via* fluid pressurization and fault weakening (Segall et al., 2010).

Experimental studies on fracture of intact samples show that dilatancy can stabilize slip events (Aben & Brantut, 2021). Moreover, measurements of volumetric changes in experimental faults (Marone et al., 1990; Samuelson et al., 2009; Proctor et al., 2020; Brantut, 2020; Aben & Brantut, 2021; Ji et al., 2022) highlight the importance of the drainage state on fluid pressure responses and show that dilatancy rate with fault slip can increase with slip velocity, which could lead to dilatancy hardening. Yet, only a few studies have successfully measured fault zone storage (Wibberley, 2002), as fault zone thickness varies greatly during slip events (Rice, 2006). These data are critical for characterizing the role of dilational processes on slip.

The purpose of this paper is to describe lab work investigating slow slip and the friction stability transition under fluid saturated conditions. Our work builds on observations of slow and complex slip (Scholz et al., 1972; Brantut et al., 2011) and studies demonstrating that complex modes of fault slip can occur when the loading stiffness K is nearly equal to the critical frictional weakening rate (or rheological stiffness) K_c (Gu et al., 1984). Laboratory studies (Leeman et al., 2016) have shown that the full spectrum of fault slip modes can occur when the loading stiffness (K) is nearly equal to the critical weakening rate, $K_c = (b - a)/D_c$, where $(b - a)$ is the friction rate parameter and D_c is the critical friction distance (Gu et al., 1984; Dieterich, 1979; Marone, 1998; Ruina, 1983). Here, we build on an extensive set of works (Leeman et al., 2015, 2016; Scuderi et al., 2016, 2017; Shreedharan et al., 2020) that document the transition from stable to unstable frictional sliding. We show that for the conditions of our experiments

95 pore pressure has a minor effect on the frictional stability transition and is not the cause
 96 of slow slip.

97 2 Experimental Methods

98 Our experiments were conducted in a true-triaxial pressure vessel (Figure 1A), using
 99 the double direct shear (DDS) configuration (Samuelson et al., 2009; Ikari et al., 2009;
 100 Kenigsberg et al., 2020). We used a synthetic fault gouge composed of quartz powder
 101 (Min-U-Sil 40) with a median grain size of 10.5 μm . Two uniform layers were constructed
 102 using a leveling jig to achieve a reproducible initial thickness of 3 mm. We weighed the
 103 layers for each experiment and ensured <10% variability between experiments (see Sup-
 104 plement Table 1). The layers were each 5.7 cm \times 5.4 cm in area. For simplicity, we re-
 105 ference all stresses, strains, and displacements to a single fault layer of the DDS arrange-
 106 ment. Total shear displacements ranged from 22–25 mm, corresponding to shear strain
 107 between 20–26. Samples were sealed in a flexible latex jacket to separate confining and
 108 pore pressures (Figure 1C).

109 Normal stress (σ_n) and shear stress (τ) are applied and maintained *via* servo-controlled
 110 hydraulic rams (Figure 1A). Upstream and downstream pore fluid pressures (P_p) and
 111 confining pressure (P_c) were independently servo-controlled. For our sample geometry
 112 (Figure 1C) fault normal stress is given by $\sigma_n + 0.63P_c$, for a Terzhagi effective normal
 113 stress, $\sigma'_n = \sigma_n + 0.63P_c - P_p$.

114 P_p is servo-controlled at a constant value and we measure both upstream and down-
 115 stream volume fluxes to determine fault perpendicular permeability. τ on the fault is ap-
 116 plied by advancing the central forcing block of the DDS arrangement at a constant dis-
 117 placement rate. Both normal and shear loads are measured by load cells with a preci-
 118 sion of 5 N (Figure 1A). Fault shear and normal displacements are measured with DCDTs
 119 external to the pressure vessel and in a few cases with DCDTs internal to the vessel; in
 120 all cases, the resolution is $\pm 0.1 \mu\text{m}$ (Figure 1B).

121 Samples were sheared with finite pore pressures between 1 and 4 MPa at 10 $\mu\text{m/s}$,
 122 and thus under fluid-saturated and drained conditions. The pore fluid of de-ionized and
 123 de-aired water was delivered to the faults *via* sintered metal frits (Figure 1B). The frits
 124 are serrated with saw-tooth faces to ensure coupling to the gouge layer. P_p was moni-
 125 tored using pressure transducers external to the pressure vessel (Figure 1A) with 0.007 MPa
 126 resolution. Loads and displacements were recorded continuously at 10 kHz sampling rates
 127 and averaged for storage from 1 Hz to 1 kHz, depending on the shear rate.

128 2.1 Sample preparation

129 The faults are sealed with a composite latex rubber membrane to isolate P_c from
 130 P_p . The seal consisted of three layers to prevent puncture during shear: (1) a 3.2 mm
 131 thick latex rubber sheet wrapped around the lower part of the sample, (2) a 0.9 mm thick
 132 latex rubber tube, and (3) a 1.5 mm thick dip-molded latex jacket for the DDS config-
 133 uration (Figure 1C).

134 2.2 Reduction of apparatus loading stiffness

135 Our goal is to study the transition from stable to unstable sliding, thus we reduced
 136 the shear loading stiffness K to match the critical weakening rate K_c . Stiffness was re-
 137 duced using two acrylic rods 42-mm in diameter and 35-mm in length in the shear load-
 138 ing column. One rod was outside the vessel at the load point and the other was inside
 139 the pressure vessel between the piston and the sample (Figure 1C). Loading stiffness cal-
 140 ibration experiments showed that P_c has a negligible effect on the spring stiffness (see
 141 Supplementary Figure 1).

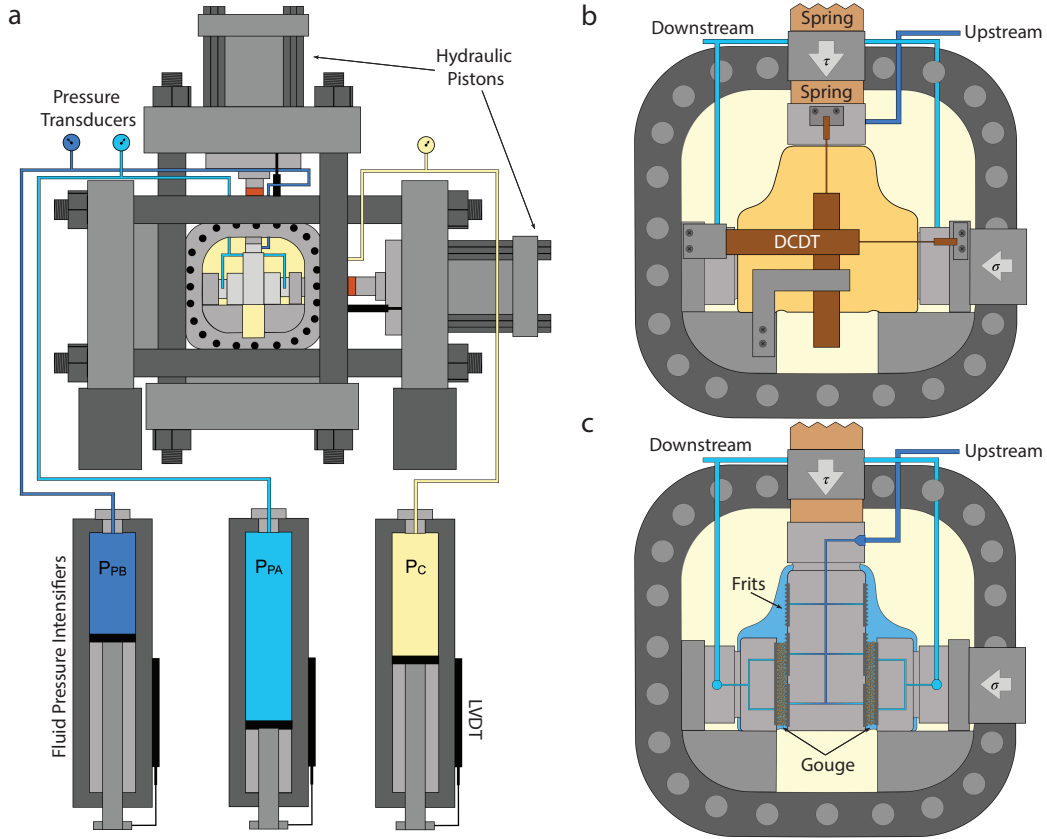


Figure 1. Schematic of the biaxial deformation apparatus and pressure vessel for true triaxial loading. (A) Two hydraulic rams apply normal and shear loads to the double direct shear (DDS) sample. Fluid intensifiers provide upstream and downstream P_p and P_c . (B) Internal DCDTs to measure fault shear and normal displacements. Two springs are placed in series with the vertical loading column to reduce stiffness. (C) We measured fault normal permeability by flowing from the central block to the side blocks of the DDS arrangement. Pore fluids enter the fault via sintered metal frits (Mott Corp.).

142

2.3 Permeability and fault zone strain

143

144

145

146

147

148

Permeability was measured every 5 mm of shear displacement with the following protocol. (1) While shearing, a constant P_p boundary condition was imposed between the upstream (PpA) and downstream (PpB) (Figure 1A). (2) The vertical piston was locked in place. (3) A 0.5 MPa P_p was imposed from PpA to PpB until the flow rates equilibrated and permeability was measured. This protocol was repeated several times throughout shear. The across-fault permeability was calculated using Darcy's law:

$$k = \frac{Q\mu L}{A\Delta P} \quad (1)$$

149

150

151

152

153

Steady-state flow was ensured by measuring upstream and downstream volume flux, where Q is the fluid discharge, μ is the water viscosity at room temperature (24°C), L is the fault layer thickness (accounting for layer compaction/dilation), A is the sample cross-sectional area, and ΔP is the pore pressure differential. Upstream and downstream values of Q differing by <5% were considered steady-state.

2.4 Experimental procedure

Experiments began by applying σ_n of 3 MPa, followed by 2 MPa P_c , after which P_p was increased to 1 MPa. Samples were saturated by (i) bleeding air from pressure lines and (ii) imposing a 0.5 MPa P_p differential across the sample to atmosphere. When constant fluid flow was achieved, (iii) P_p was increased to 1 MPa, and the bleed valve was closed. At this point, upstream and downstream P_p values were equalized, followed by final check for trapped air.

After saturation, σ_n was increased to the target stress (18–21 MPa) and P_c was increased to 5 MPa. During this compaction stage, P_p was increased to the target value (1–4 MPa). Experiments began with a permeability measurement, after compaction, followed by a 10 $\mu\text{m/s}$ shear loading segment with a shear unload/reload stage at 3 and 6 mm to promote comminution and steady-state shear fabric (Figure 3A). We sheared samples for up to 25 mm, and then locked the vertical piston and made a final permeability measurement (Figure 1B).

3 Results

Stress-displacement curves for our experiments show a consistent behavior of linear shear stress increase followed by gradual yield (Figure 2). After the shear load cycles we observe a period of stable sliding followed by emergent, quasi-periodic unstable slow-slip (Figure 2A). The stick-slip events are laboratory analogs of earthquakes. The labquakes are slow and complex initially, and reach a steady-state that is dictated by K and K_c . Samples typically reached peak friction at shear strains ranging from 7–9. After the slide-hold-slide test at 10 mm, sliding transitions from stable motion to quasi-unstable motion with small-amplitude oscillations that grow over 10–20 slip cycles (Figure 2B).

A separate suite of experiments were used to measure permeability evolution as a function of strain. Permeability evolved from 10^{-17} to 10^{-19} m^2 (see Supplementary Figure 2), with the greatest decrease occurring from 0–10 shear strain. Once the fault reached steady-state friction, permeability changes were small (see Supplementary Figure 2).

3.1 Lab earthquake measurements

For each slip event, we measured the co-seismic and inter-seismic periods using the maximum and minimum shear stress to define the beginning and end of failure. (Figure 2C, see Supplementary Figure 4). Stress drop was measured as the difference between the maximum shear stress before failure and the minimum shear stress after slip. Stress drops ranged from 0.01 to 0.65 MPa. Slip velocity was calculated using a 0.1 μm displacement-based moving window of the on-fault displacement. Peak slip velocities ranged from just above the background loading rate (10 $\mu\text{m/s}$) for slow events to 1100 $\mu\text{m/s}$ for the fastest events. Slip event durations ranged from 0.3 to 7 s. Shear loading stiffness K was measured from (1) unloading/reloading cycles and (2) a linear fit to the shear stress curves during the locked (linear elastic) section of the seismic cycle (see Supplementary Figure 3).

3.2 Lab earthquakes with finite pore pressure

Experiments show a consistent pattern of stable sliding that transitions to stick-slip behavior and lab earthquakes after shear strains of 12 to 14 (Figure 3). The suite of experiments shows minor differences in frictional strength and strain weakening behavior (see Supplementary Figure 5), with peak friction ranging from 0.54 to 0.7. The transition from stable sliding to quasi-periodic slow-slip occurs at lower shear strains (11–13) for higher P_p (Figure 3). Despite the effect of P_p on stick-slip initiation, there is

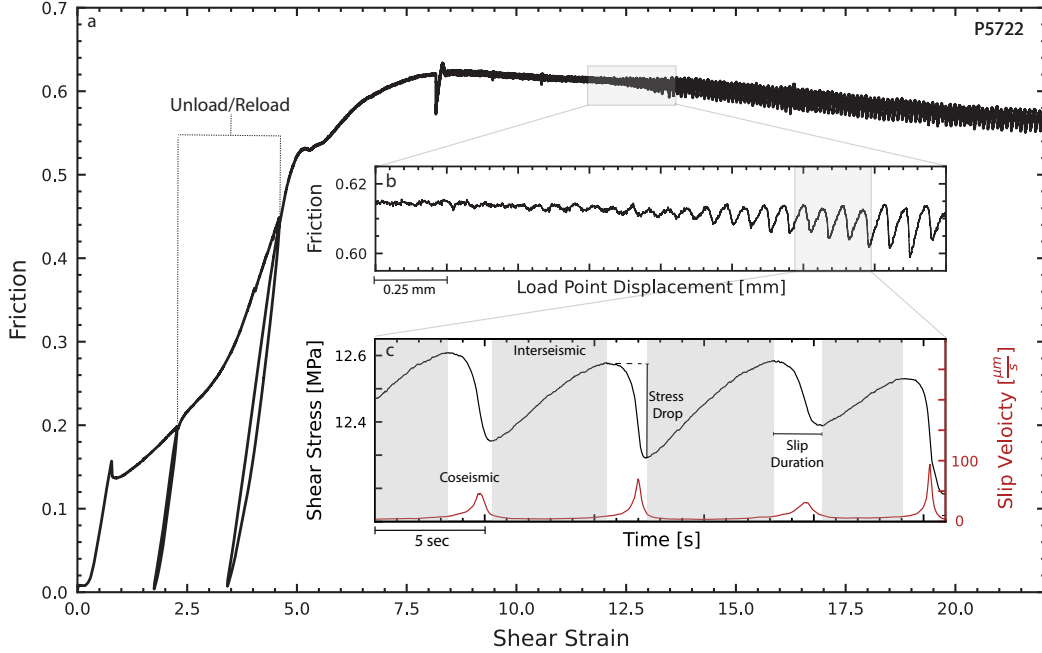


Figure 2. Data for one complete experiment showing fault zone shear stress and shear strain derived from shear displacement and fault thickness. (A) Steady-state friction was reached by shear strains of 7-9. (B) The transitions from stable sliding to slow periodic stick-slips occurred over a small displacement range and 10 - 20 seismic cycles. (C) For each stick-slip event, the co- and inter-seismic periods were defined via the shear stress. We measure stress drop, slip duration and slip velocity for each event. Shear loading stiffness was measured from the friction displacement curve during the locked stage of each event (see Supplementary Figure 3).

201 no clear correlation with the rate at which events reach a steady limit-cycle of labquake
 202 failure events, which we define as $< 10\%$ change in stress drop over a few mm of slip.
 203 We assume that steady-state labquake repeat times and stress drops are the result of reach-
 204 ing a steady fault zone shear fabric.

205 The transition from stable sliding to quasi-periodic slow-slip under fluid saturated
 206 conditions is quite similar to that observed in previous works without pore fluids (Scuderi
 207 et al., 2017; Leeman et al., 2016; Shreedharan et al., 2020). This stage typically has small
 208 amplitude modulations in shear stress of 10s of kPa and slip velocity just above back-
 209 ground loading velocity. Periods of stable sliding and oscillatory modulation generally
 210 occur over the same shear displacement length scales (Figure 3A). There is no appar-
 211 ent correlation between the number of small amplitude modulations and when the fault
 212 transitions from stable sliding to quasi-periodic slow-slip. The transition from stable to
 213 unstable slip occurs during a period of small amplitude oscillations, and while the inter-
 214 seismic period remains near-constant the stress drop magnitude increases over 20 - 50
 215 events before a steady-state stick-slip cycle is achieved. Over this range, labquake cy-
 216 cles have stress drops < 0.2 MPa and slip velocities < 100 $\mu\text{m}/\text{s}$. The co-seismic slip du-
 217 ration scales inversely with peak fault slip velocity (Figure 3B). For the transitory stage
 218 between stable and unstable slip, we note that the onset of failure is often irregular and
 219 difficult to identify, which could explain the data scatter (Figure 3C). As slip events be-
 220 come larger in magnitude and faster the fault creep rate during the interseismic period
 221 decreases systematically (see Supplementary Figure 6), matching previous works on the

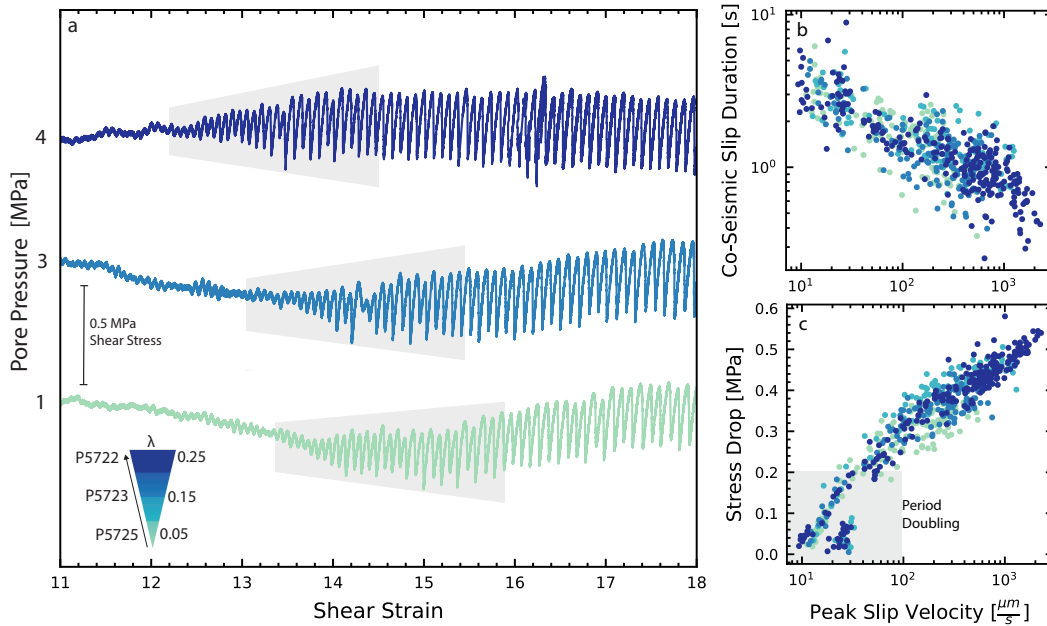


Figure 3. (a) Stick-slip event characteristics for experiments at 3 different pore pressures. Shear stress is plotted vs. shear strain during the transition from stable to unstable slip. The transition from small instabilities to quasi-periodic labquakes occurs over a few slip cycles (grey boxes). Panels (b) and (c) show event data for shear strains from 12 to 20 for our complete data set. Stick-slip events evolve from slow to fast, with a log-linear relationship between stress drop and slip velocity. Larger events, with bigger stress drops, reach peak fault slip velocity >1 mm/s with the largest stress drops and corresponding fastest events occurring at the highest λ values. Note the clear trend between co-seismic slip duration and stress drop.

222 relationship between stress drop and creep rate (Shreedharan et al., 2023). In addition,
 223 the co-seismic slip duration decreases during this stage. While friction reaches a quasi-
 224 steady state by shear strains of about 15, labquake stress drops continue to grow, go-
 225 ing from 0.2 to 0.6 MPa with peak slip velocities going from 100 to 1100 $\mu\text{m}/\text{s}$.

226 3.3 Effect of loading stiffness on fault stability

227 For our apparatus, the transition from stable to unstable motion occurs when load-
 228 ing stiffness K is ≈ 0.015 MPa/ μm (Leeman et al., 2015, 2016; Scuderi et al., 2016; Shree-
 229 dharan et al., 2020). The effective stiffness increases initially upon loading as the fault
 230 zone compacts but then does not change appreciably after steady-state friction is reached.
 231 The onset of slow, quasi-periodic labquakes occurs at a low value of K and evolves over
 232 a shear strain of 5–8 (Figure 4). This initial stage hosts complex slip behaviors includ-
 233 ing period doubling. Once steady-state stick-slip is achieved, K then increases at a much
 234 slower rate. Consistent with previous work, lower values of K produce larger events with
 235 bigger stress drop and higher slip velocity (Leeman et al., 2016; Rudolf et al., 2021). Event
 236 sizes and magnitudes continue to evolve as a function of strain, with more dynamic events
 237 occurring at progressively higher shear strains (Scuderi et al., 2017, 2020).

238 The stability transition occurs when K becomes $< K_c$, and we observe that both
 239 K and K_c evolve with shear strain. We present two estimates for the K_c envelope (Fig-

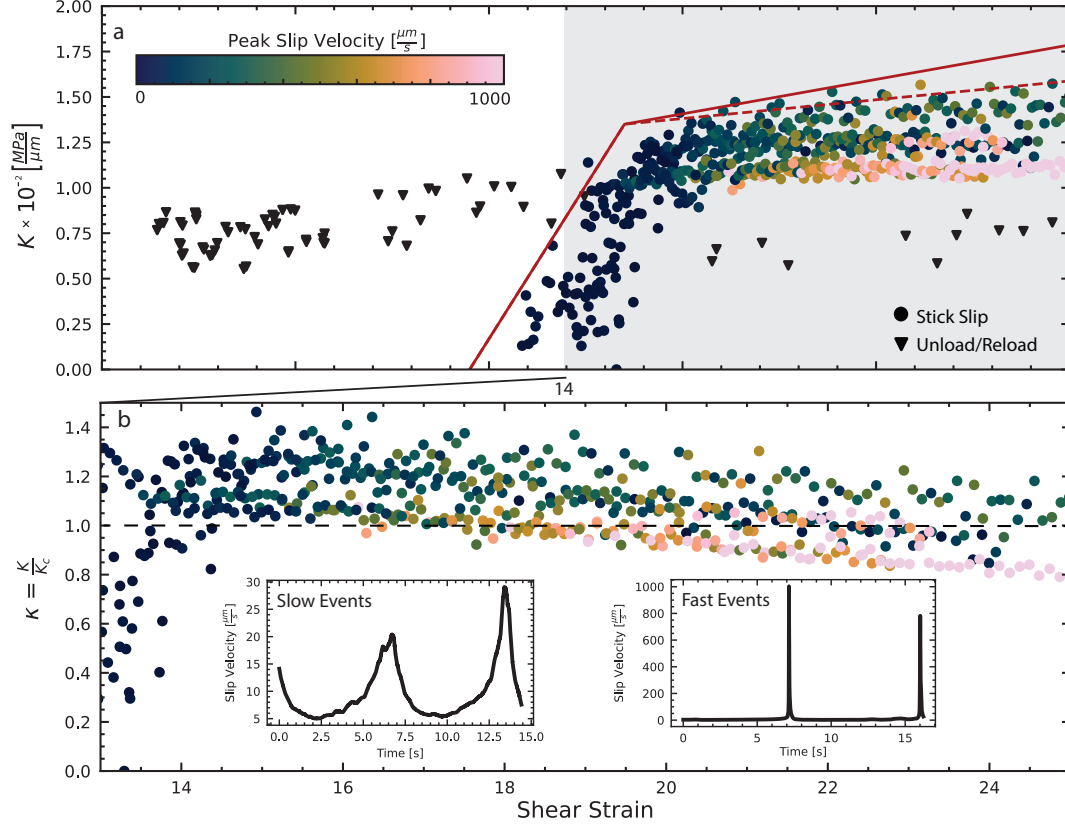


Figure 4. Loading stiffness K measured from experiments at 20 MPa σ'_n and P_p from 1 - 4 MPa (Supplement Table). (a). Data points show K values measured from unload-reload cycles and stick-slip. Lines show the evolution of K_c with shear strain; the solid line is the preferred model, dashed line shows an alternative model. Note that the transition from stable to unstable slip occurs at a shear strain of ≈ 14 (see also Fig. 1). (b) Zoom of the shaded portion of Panel A showing stick-slip evolution from slow to fast slip events, as predicted by theory when data fall below the dashed line showing $\kappa = 1$. Insets shows detail of slip velocity history during slow and fast events at shear strain of 15 and 22, respectively.

240 ure 4A). Both thresholds are determined from RSF parameters and a theoretical envelope
 241 based on stress dependence of frictional stability (Leeman et al., 2016; Scuderi et
 242 al., 2016). The first (dashed line) assumes minimal rheological evolution, such that K_c
 243 is roughly constant with shear and small changes in K are the cause of changes in event
 244 size (Gu et al., 1984; Leeman et al., 2016). Conversely, the second (solid line) shows a
 245 small evolution of K_c , consistent with lab data (Scuderi et al., 2017). The solid line ac-
 246 counts for small changes in frictional properties and their impact on instability. Because
 247 σ'_n is constant, K remains nearly constant throughout the experiment, changing only dur-
 248 ing initial shear when the fault zone compacts and stiffens. Such changes in the effec-
 249 tive loading stiffness with strain are linked to densification and shear fabric development.
 250 However, increases in K_c with strain typically outpace changes in K . Therefore, once
 251 the critical stiffness ratio is reached, with ($\kappa = K/K_c \approx 1$), the evolution of event mag-
 252 nitude is primarily modulated *via* the rheological weakening rate K_c . We find that slow
 253 events correspond to κ values from 1.4 - 1.1, whereas faster, more dynamic events typ-

254 ically have κ below 1. The relation between κ and shear strain outpaces the effects of
 255 λ , such that all experiments follow a similar evolution from slow to fast regardless of P_p .

256 4 Discussion

257 P_p can affect the mode of frictional sliding *via* σ'_n and/or fluid drainage state as
 258 controlled by permeability and the rate of shearing rate and porosity change. The sta-
 259 bility transition from stable to unstable sliding depends on σ'_n and P_p . Thus, changes
 260 in P_p could produce a change in stability by reducing the fault stress, which in isolation
 261 would tend to promote slow-slip and stable sliding. Another possibility is that quasi-dynamic
 262 changes in fault zone porosity could produce dilatant strengthening or, the opposite, weak-
 263 ening *via* fluid pressurization (Segall & Rice, 2006; Segall et al., 2010; Brantut, 2020).
 264 Our experiments test the assumption that pore fluid pressure alone is the driving mech-
 265 anism for complex modes of fault slip. We explore how slow-slip can occur under finite
 266 P_p , even in cases where dilatancy strengthening is negligible, highlighting that it depends
 267 not only on the presence of pore fluids - but also on the magnitude of pore pressure and
 268 complexity of fluid pathways.

269 4.1 The effect of fluid pressure on lab earthquakes

270 Our results demonstrate that the stability transition from stable to unstable mo-
 271 tion occurs gradually (Figure 2A) followed by evolution from slow and complex slip events
 272 to steady, quasi-periodic labquakes over 10 - 20 lab seismic cycles (Figure 3A). Instabil-
 273 ities nucleate at somewhat lower shear strain for higher λ , but with negligible effect on
 274 labquake stress drop or recurrence interval. For our range of P_p values the effective load-
 275 ing stiffness K is the same and we see similar behaviors, indicating that P_p has a minor
 276 effect on slip behavior (Figure 4A).

277 Importantly, our results indicate that under constant pressure conditions at low
 278 P_p , there is minimal effect on labquake initiation and evolution. We measured pore-pressure
 279 near the fault surface but not directly on it, which allows the possibility that dilatational
 280 mechanisms existed but were potentially masked by measurement volume effects (Brantut,
 281 2020). While we cannot rule this out completely, we note that our results are consistent
 282 with previous work using similar materials and absent of fluids (Leeman et al., 2016; Scud-
 283 eri et al., 2016). These studies show that slow-slip and complex slip behaviors near the
 284 stability boundary are caused by velocity-dependent changes in the critical frictional weak-
 285 ening rate. With the consideration in mind, our results indicate that at low P_p condi-
 286 tions slow-slip is not produced by dilatational mechanisms.

287 Previous works have documented the transition from stable to unstable stick-slip
 288 (Figure 2) as a function of stiffness (Leeman et al., 2016; Rudolf et al., 2021) by match-
 289 ing the effective loading stiffness K to the critical loading stiffness K_c , (Gu et al., 1984)
 290 such that $\kappa = K/K_c \leq 1$. The evolution of spontaneous stick-slips is widely agreed
 291 to depend on shear fabric evolution (Scuderi et al., 2017, 2020; Bedford & Faulkner, 2021)
 292 - where the RSF parameters continue to evolve such that K_c outpaces any increase in
 293 K sample compaction and geometric thinning of gouge.

294 Our results indicate that regardless of pore pressure, instabilities nucleate in the
 295 same envelope of K_c as previous studies (Leeman et al., 2016; Scuderi et al., 2017). This
 296 suggests that dilatant volume changes are minor and occur under drained fluid condi-
 297 tions. Importantly, we find that stick-slip magnitude increases as a function of shear strain
 298 (Figure 4A). The strain-dependent evolution of K_c has two mechanisms: (1) the dashed
 299 line assumes K is the driving mechanism for instabilities, where once the material reaches
 300 steady-state sliding, events should not change, or (2) the solid line suggests that shear
 301 strain sensitive processes, such as grain size reduction (Niemeijer et al., 2009, 2010; Col-
 302 lettini et al., 2011; Bedford & Faulkner, 2021), dictate how and when a fault will nucle-

303 ate laboratory stick-slip cycles. We posit that at constant stress conditions, when vol-
 304 umetric changes, and thus P_p are sufficiently small, shear fabric evolution is the driv-
 305 ing mechanism promoting fault instability. We cannot rule out a role of P_p in natural
 306 fault systems, it seems likely that slow slip is caused by more than just pore fluids.

307 4.2 Fluid diffusion time and fault stability

308 Under fluid-saturated conditions, the stress dependence of frictional behavior and
 309 RSF parameters (a, b, D_c) depend on fault zone volume changes *via* dilation/compaction
 310 and the fluid diffusion time. Recent friction studies at higher pore pressure and also stud-
 311 ies of rock fracture show that fault dilation can result in significant P_p transients (Brantut,
 312 2020; Aben & Brantut, 2021). These experiments documented undrained conditions and
 313 local reduction of P_p . We evaluated the possibility that our experiments also involved
 314 undrained loading. We did this by comparing pore fluid volume changes with changes
 315 in layer thickness, following previous work (Samuelson et al., 2009). This comparison shows
 316 that our loading conditions were drained. The measured changes in layer thickness agree
 317 well with the pore volume measurements for our full range of conditions.

318 In other works, the evolution of fault zone permeability has been related to changes
 319 in porosity (Crawford et al., 2008; Faulkner et al., 2018) due to grain size reduction dur-
 320 ing shearing (Niemeijer et al., 2010; Collettini et al., 2011; Bedford & Faulkner, 2021).
 321 These work also suggest an increase in complexity of the fluid pathways due to shear fab-
 322 ric evolution perpendicular to the flow direction (Zhang et al., 1999). In this case, the
 323 characteristic drainage time due to the internal generation of pore fluid pressures is,

$$t = \frac{L^2 \eta * (\beta_p + \Phi \beta_w)}{2k} \quad (2)$$

324 where L is layer thickness, η is dynamic fluid viscosity, ϕ is porosity, k is perme-
 325 ability and β_p and β_w are the compressibility of the porous medium and fluid. For our
 326 experiments Equation 2 gives a fluid diffusion time of the order of 1 second, which is con-
 327 sistent with our measurements of porosity and layer thickness change (see Supplemen-
 328 tary Figure 7). Thus, a shearing rate of 10 $\mu\text{m/s}$ would sustain localized over-pressure
 329 or under-pressure – effectively weakening, or strengthening the fault. Within this frame-
 330 work, shear-induced changes in P_p are controlled by changes in fault volume and the du-
 331 ration of these effects would increase as permeability decreases. Therefore, at the same
 332 loading velocity, the permeability-shear strain evolution is the primary mechanism con-
 333 trolling P_p - slip responses. Critical to our study, is the minor impact of these local mech-
 334 anisms on the bulk laboratory seismic cycle.

335 Importantly, our study demonstrates that at low P_p , despite the fault hosting in-
 336 stances of undrained fluid pressure, there is no resolvable effect on fault slip or stress drop.
 337 When fluid effects are important, fault weakening or strengthening is rate-controlled by
 338 fluid diffusion (Paola et al., 2007), the fault plane will experience periodic increased or
 339 decreased frictional strength based on the sense of porosity change (Sibson, 1986; Segall
 340 et al., 2010) - compactive or dilational. Our results demonstrate that across low P_p con-
 341 ditions, frictional processes alone are sufficiently explain stick-slip evolution. We postu-
 342 late that not only high pore pressures, but significantly anisotropic permeability is re-
 343 quired to elucidate the complex slip phenomena observed in nature.

344 5 Conclusion

345 We conducted well-controlled frictional shearing experiments to explore the origin
 346 of slow-slip and the frictional stability transition for conditions of finite pore pressure.
 347 We tested the hypothesis that slow slip is caused by changes in fluid pressure and dila-
 348 tancy strengthening associated with undrained conditions. Our results show that this

349 hypothesis must be rejected. Instead, our data are consistent with the interpretation that
 350 the slow slip and complex modes of frictional sliding arise from variation of the rate of
 351 frictional weakening K_c as a function of slip velocity. Our data show that the transition
 352 from stable sliding to first quasi-periodic slow-slip and eventually elasto-dynamic fast
 353 labquakes is linked to changes in frictional properties that arise from shear fabric devel-
 354 opment. We conclude that elevated P_p and drainage-limited conditions, are required to
 355 activate dilational mechanisms controlling slip. We find that slow-slip and complex modes
 356 of fault motion can occur under finite P_p without dilatancy strengthening or undrained
 357 loading conditions.

358 Data Availability Statement

359 All data are available at <https://doi.org/10.5281/zenodo.7734607>.

360 Acknowledgments

361 We thank Steven Swavelly for laboratory technical support and Drs. Srisharan Shreed-
 362 haran, David (Chas) Bolton, Marco Scuderi, and Carolina Giorgetti for scientific sup-
 363 port and discussions. This work was supported by US Department of Energy grants DE-
 364 SC0020512 and DE-EE0008763 and European Research Council Advance Grant 835,012
 365 (TECTONIC).

366 References

- 367 Aben, F., & Brantut, N. (2021). Dilatancy stabilises shear failure in rock. *Earth and*
 368 *Planetary Science Letters*, *574*, 1–34. doi: 10.1016/j.epsl.2021.117174
- 369 Bedford, J. D., & Faulkner, D. R. (2021). The role of grain size and effective normal
 370 stress on localization and the frictional stability of simulated quartz gouge.
 371 *Geophysical Research Letters*, *48*(7), e2020GL092023.
- 372 Behr, W., & Bürgmann, R. (2021). What’s down there? the structures, mate-
 373 rials and environment of deep-seated slow slip and tremor. *Philosophical*
 374 *Transactions of the Royal Society A: Mathematical, Physical and Engineering*
 375 *Sciences*, *379*(2193). doi: 10.1098/rsta.2020.0218
- 376 Biot, M. (1941). General theory of three-dimensional consolidation. *Journal of Ap-*
 377 *plied Physics*, *12*(2), 155-164. doi: 10.1063/1.1712886
- 378 Brantut, N. (2020). Dilatancy-induced fluid pressure drop during dynamic rup-
 379 ture: Direct experimental evidence and consequences for earthquake dy-
 380 namics. *Earth and Planetary Science Letters*, *538*, 1–25. doi: 10.1016/
 381 j.epsl.2020.116179
- 382 Brantut, N., Sulem, J., & Schubnel, A. (2011). Effect of dehydration reac-
 383 tions on earthquake nucleation: Stable sliding, slow transients, and un-
 384 stable slip. *Journal of Geophysical Research: Solid Earth*, *116*(B5). doi:
 385 10.1029/2010JB007876
- 386 Bürgmann, R. (2018). The geophysics, geology and mechanics of slow fault slip.
 387 *Earth and Planetary Science Letters*, *495*, 112–134. doi: 10.1016/j.epsl.2018.04
 388 .062
- 389 Collettini, C., Niemeijer, A., Viti, C., Smith, S., & Marone, C. (2011). Fault struc-
 390 ture, frictional properties and mixed-mode fault slip behavior. *Earth and Plan-*
 391 *etary Science Letters*, *311*(3-4), 316–327.
- 392 Condit, C., & French, M. (2022). Geologic evidence of lithostatic pore fluid pressures
 393 at the base of the subduction seismogenic zone. *Geophysical Research Letters*,
 394 *49*(12), e2022GL098862.
- 395 Crawford, B., Faulkner, D., & Rutter, E. (2008). Strength, porosity, and permeabil-
 396 ity development during hydrostatic and shear loading of synthetic quartz-clay
 397 fault gouge. *Journal of Geophysical Research: Solid Earth*, *113*(B3).

- 398 Dal Zilio, L., Lapusta, N., & Avouac, J.-P. (2020). Unraveling scaling properties of
399 slow-slip events. *Geophysical Research Letters*, *47*(10), e2020GL087477.
- 400 Dieterich, J. (1979). Modeling of rock friction 1. experimental results and consti-
401 tutive equations. *Journal of Geophysical Research: Solid Earth*, *84*(B5), 2161–
402 2168. doi: 10.1029/JB084iB05p02161
- 403 Ellsworth, W. (2013). Injection-induced earthquakes. *Science*, *341*(6142), 1225942.
404 doi: 10.1126/science.1225942
- 405 Faulkner, D., & Rutter, E. (2001). Can the maintenance of overpressured fluids in
406 large strike-slip fault zones explain their apparent weakness? *Geology*, *29*(6),
407 503–506.
- 408 Faulkner, D., Sanchez-Roa, C., Boulton, C., & Den Hartog, S. (2018). Pore fluid
409 pressure development in compacting fault gouge in theory, experiments, and
410 nature. *Journal of Geophysical Research: Solid Earth*, *123*(1), 226–241.
- 411 Gu, J., Rice, J., Ruina, A., & Tse, S. (1984). Slip motion and stability of a single
412 degree of freedom elastic system with rate and state dependent friction. *Jour-
413 nal of the Mechanics and Physics of Solids*, *32*(3), 167–196. doi: 10.1016/0022-
414 -5096(84)90007-3
- 415 Hubbert, K., & Rubey, W. (1959). Role of fluid pressure in mechanics of
416 overthrust faulting: I. mechanics of fluid-filled porous solids and its ap-
417 plication to overthrust faulting. *GSA Bulletin*, *70*(2), 115-166. doi:
418 10.1130/0016-7606(1959)70[115:ROFPIM]2.0.CO;2
- 419 Ikari, M., Saffer, D., & Marone, C. (2009). Frictional and hydrologic properties of
420 clay-rich fault gouge. *Journal of Geophysical Research: Solid Earth*, *114*(B5).
421 doi: 10.1029/2008JB006089
- 422 Ji, Y., Hofmann, H., Rutter, E., & Zang, A. (2022). Transition from slow to fast
423 injection-induced slip of an experimental fault in granite promoted by elevated
424 temperature. *Geophysical Research Letters*, *49*(23), e2022GL101212.
- 425 Kenigsberg, A., Rivière, J., Marone, C., & Saffer, D. (2020). Evolution of elastic
426 and mechanical properties during fault shear: The roles of clay content, fabric
427 development, and porosity. *Journal of Geophysical Research: Solid Earth*,
428 *125*(3), 1–16. doi: 10.1029/2019JB018612
- 429 Leeman, J., Saffer, D., Scuderi, M., & Marone, C. (2016). Laboratory observa-
430 tions of slow earthquakes and the spectrum of tectonic fault slip modes. *Nature
431 Communications*, *7*, 1–6. doi: 10.1038/ncomms11104
- 432 Leeman, J., Scuderi, M., Marone, C., & Saffer, D. (2015). Stiffness evolution of gran-
433 ular layers and the origin of repetitive, slow, stick-slip frictional sliding. *Granu-
434 lar Matter*, *17*(4), 447–457. doi: 10.1007/s10035-015-0565-1
- 435 Marone, C. (1998). Laboratory-derived friction laws and their application to seismic
436 faulting. *Annual Review of Earth and Planetary Sciences*, *26*(1), 643-696. doi:
437 10.1146/annurev.earth.26.1.643
- 438 Marone, C., Raleigh, C., & Scholz, C. (1990). Frictional behavior and constitutive
439 modeling of simulated fault gouge. *Journal of Geophysical Research*, *95*, 7007-
440 7025. doi: 10.1029/JB095iB05p07007
- 441 Niemeijer, A., Elsworth, D., & Marone, C. (2009). Significant effect of grain size dis-
442 tribution on compaction rates in granular aggregates. *Earth and Planetary Sci-
443 ence Letters*, *284*(3-4), 386–391.
- 444 Niemeijer, A., Marone, C., & Elsworth, D. (2010). Frictional strength and strain
445 weakening in simulated fault gouge: Competition between geometrical weaken-
446 ing and chemical strengthening. *Journal of Geophysical Research: Solid Earth*,
447 *115*(10), 1–16. doi: 10.1029/2009JB000838
- 448 Paola, N. D., Collettini, C., Trippetta, F., Barchi, M. R., & Minelli, G. (2007).
449 A mechanical model for complex fault patterns induced by evaporite dehy-
450 dration and cyclic changes in fluid pressure. *Journal of Structural Geology*,
451 *29*(10), 1573-1584. Retrieved from [https://www.sciencedirect.com/
452 science/article/pii/S0191814107001411](https://www.sciencedirect.com/science/article/pii/S0191814107001411) doi: <https://doi.org/10.1016/>

- 453 j.jsg.2007.07.015
- 454 Proctor, B., Lockner, D., Kilgore, B., Mitchell, T., & Beeler, N. (2020). Direct
455 evidence for fluid pressure, dilatancy, and compaction affecting slip in isolated
456 faults. *Geophysical Research Letters*, *47*(16). doi: 10.1029/2019GL086767
- 457 Rice, J. (2006). Heating and weakening of faults during earthquake slip. *Journal of*
458 *Geophysical Research: Solid Earth*, *111*(B5). doi: 10.1029/2005JB004006
- 459 Rudolf, M., Rosenau, M., & Oncken, O. (2021). The spectrum of slip behaviors of
460 a granular fault gouge analogue governed by rate and state friction. *Geochem-*
461 *istry, Geophysics, Geosystems*, *22*(12), e2021GC009825.
- 462 Ruina, A. (1983). *Slip instability and state variable friction laws* (Vol. 88)
463 (No. B12). doi: 10.1029/JB088iB12p10359
- 464 Sacks, I. S., Linde, A. T., Suyehiro, S., & Snoke, J. A. (1978). Slow earthquakes and
465 stress redistribution. *Nature*, *275*(5681), 599–602.
- 466 Samuelson, J., Elsworth, D., & Marone, C. (2009). Shear-induced dilatancy of fluid-
467 saturated faults: Experiment and theory. *Journal of Geophysical Research:*
468 *Solid Earth*, *114*(12), 1–15. doi: 10.1029/2008JB006273
- 469 Scholz, C., Molnar, P., & Johnson, T. (1972). Detailed studies of frictional sliding of
470 granite and implications for the earthquake mechanism. *Journal of geophysical*
471 *research*, *77*(32), 6392–6406.
- 472 Scuderi, M., Collettini, C., Vitti, C., Tinti, E., & Marone, C. (2017). Evolution of
473 shear fabric in granular fault gouge from stable sliding to stick slip and impli-
474 cations for fault slip mode. *Geology*, *45*(8), 731–734. doi: 10.1130/G39033.1
- 475 Scuderi, M., Marone, C., Tinti, E., Di Stefano, G., & Collettini, C. (2016). Precu-
476 ratory changes in seismic velocity for the spectrum of earthquake failure modes.
477 *Nature Geoscience*, *9*(9), 695–700. doi: 10.1038/ngeo2775
- 478 Scuderi, M., Tinti, E., Cocco, M., & Collettini, C. (2020). The role of shear fabric in
479 controlling breakdown processes during laboratory slow-slip events. *Journal of*
480 *Geophysical Research: Solid Earth*, *125*(11), e2020JB020405.
- 481 Segall, P., & Rice, J. (2006). Does shear heating of pore fluid contribute to earth-
482 quake nucleation? *Journal of Geophysical Research: Solid Earth*, *111*(B9).
- 483 Segall, P., Rubin, A., Bradley, A., & Rice, J. (2010). Dilatant strengthening as a
484 mechanism for slow slip events. *Journal of Geophysical Research: Solid Earth*,
485 *115*(12), 1–37. doi: 10.1029/2010JB007449
- 486 Shreedharan, S., Bolton, D., Rivière, J., & Marone, C. (2020). Preseismic fault creep
487 and elastic wave amplitude precursors scale with lab earthquake magnitude for
488 the continuum of tectonic failure modes. *Geophysical Research Letters*, *47*(8),
489 1–10. doi: 10.1029/2020GL086986
- 490 Shreedharan, S., Saffer, D., Wallace, L., & Williams, C. (2023). Ultralow frictional
491 healing explains recurring slow slip events. *Science*, *379*(6633), 712–717. Re-
492 trieved from <https://www.science.org/doi/abs/10.1126/science.adf4930>
493 doi: 10.1126/science.adf4930
- 494 Sibson, R. (1986). Earthquakes and rock deformation in crustal fault zones. *Annual*
495 *Review of Earth and Planetary Sciences*, *14*(1), 149–175. doi: 10.1146/annurev
496 .ea.14.050186.001053
- 497 Wibberley, C. (2002). Hydraulic diffusivity of fault gouge zones and implications for
498 thermal pressurization during seismic slip. *Earth, Planets and Space*, *54*(11),
499 1153–1171. doi: 10.1186/BF03353317
- 500 Williams, R. (2019). Coseismic boiling cannot seal faults: Implications for the seis-
501 mic cycle. *Geology*, *47*(5), 461–464. doi: 10.1130/G45936.1
- 502 Zhang, S., Tullis, T., & Scruggs, V. (1999). Permeability anisotropy and pressure
503 dependency of permeability in experimentally sheared gouge materials. *Journal*
504 *of structural geology*, *21*(7), 795–806.

Figure1.

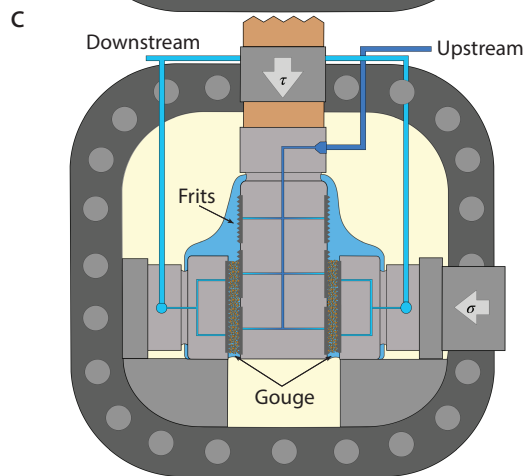
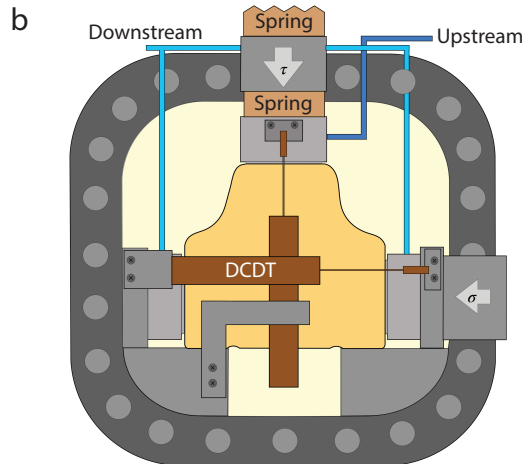
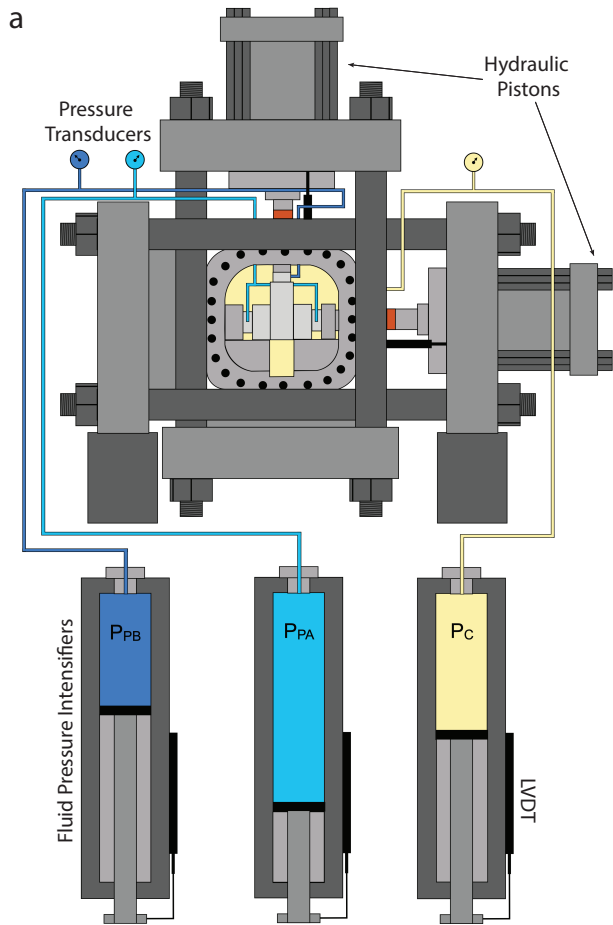


Figure2.

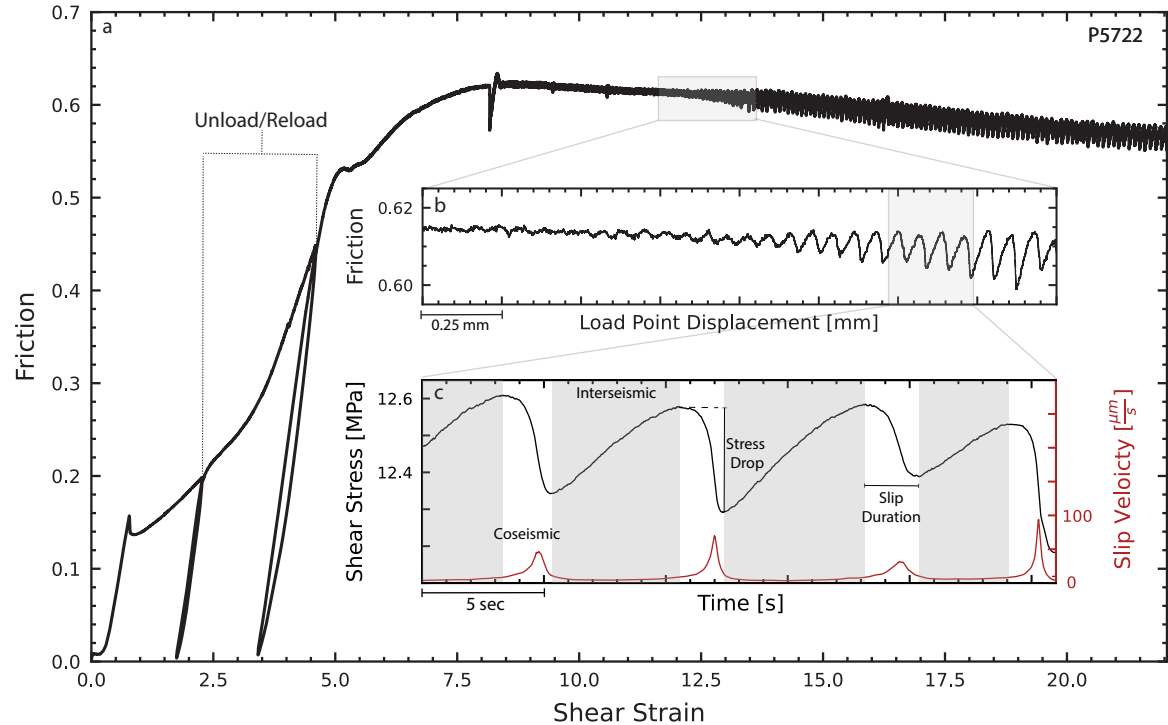


Figure3.

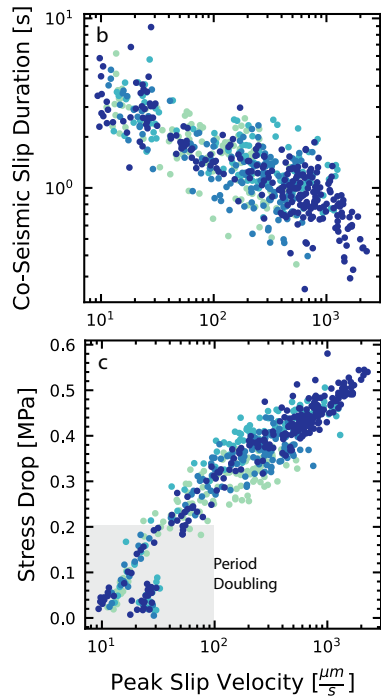
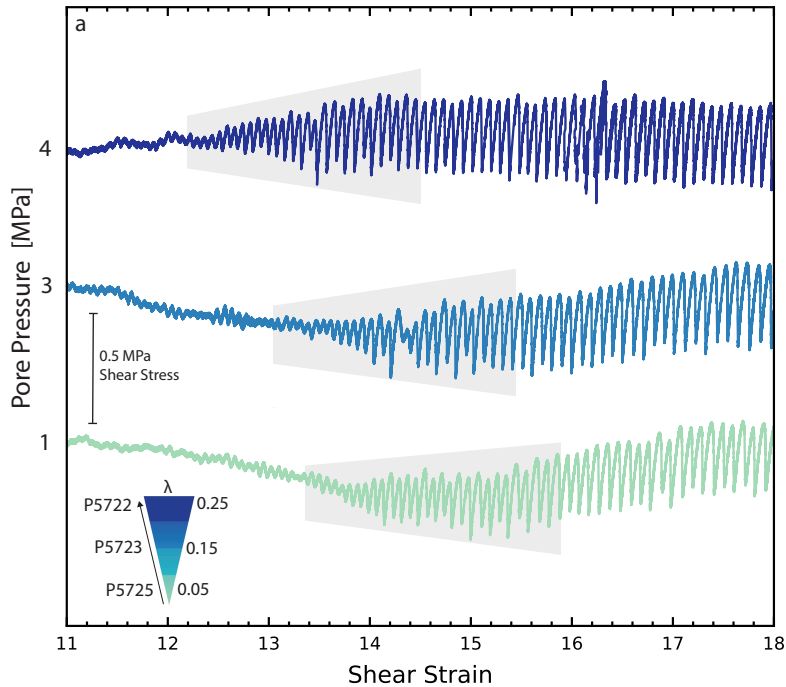


Figure4.

